Helical flow in three-dimensional nonstationary anisotropic heterogeneous porous media

Gabriele Chiogna[1], Olaf A. Cirpka[1], Massimo Rolle[1,2], and Alberto Bellin[3]

[1]Center for Applied Geoscience, University of Tübingen, Tübingen, Germany, [2]Department of Civil and Environmental Engineering, Stanford University, Stanford, California, USA, [3]Department of Civil, Environmental and Mechanical Engineering, University of Trento, Trento, Itlay

Abstract Characterizing the topology of three-dimensional steady-state flow fields is useful to describe the physical processes controlling the deformation of solute plumes and, consequently, obtain helpful information on mixing processes without solving the transport equation. In this work, we study the topology of flow in three-dimensional nonstationary anisotropic heterogeneous porous media. In particular, we apply a topological metric, i.e., the helicity density, and two complementary kinematic descriptors of mixing, i.e., stretching and folding, to investigate: (i) the flow field resulting from applying a uniform-in-the-average hydraulic gradient within a fully resolved heterogeneous three-dimensional porous medium with a nonstationary anisotropic covariance function of the locally isotropic hydraulic log conductivity; (ii) the flow field obtained by averaging a set of Monte Carlo realizations of the former field; (iii) the flow field obtained considering the blockwise uniform anisotropic effective conductivity tensor computed for the fully resolved case. While in the fully resolved case, the local helicity density is zero as a consequence of the local isotropy of hydraulic conductivity, it differs from zero in the other two cases. We show, therefore, that this topological metric is scale dependent and should be computed at the appropriate scale to be informative about the leading patterns of plume deformation. Indeed, streamlines are helical in all three cases at scales larger than the characteristic scale of spatial variability. We apply stretching and folding metrics to investigate the scales at which plume deformation is more influenced by helical motion than by the effect of small-scale spatial heterogeneity in the hydraulic-conductivity field. Under steady-state flow conditions, stretching, which quantifies the increasing length of an interface, dominates at short distances from a given starting plane, while folding, which describes how this interface is bent to fill a finite volume of space, dominates further downstream and can be correlated with the appearance of large-scale secondary motion. We conclude that three-dimensional flows in porous media may show a complex topology whose analysis is relevant for the description of plume deformation. These results have important implications for the understanding of mixing processes, as shown in detail in the companion paper focusing on solute transport.

1. Introduction

A correct parameterization of hydraulic conductivity is of critical importance for the description of flow and transport in porous media since it determines the geometry and topology of streamlines [*Sposito*, 1994, 2001; *Sposito and Weeks*, 1998; *Chiogna et al.*, 2014], solute dilution [*de Barros et al.*, 2012; *Le Borgne et al.*, 2010, 2013; *Cirpka et al.*, 2011; *Kitanidis*, 1994; *Rolle et al.*, 2013; *Rolle and Kitanidis*, 2014], and mixing enhancement [*Werth et al.*, 2006; *Rolle et al.*, 2009; *Chiogna et al.*, 2011a, 2012]. However, due to the inherent complexity of natural porous formations, a fully-resolved description of the conductivity field is often neither possible nor necessary to describe larger-scale flow structures. Upscaling heterogeneous properties is a classical problem in many branches of physics [e.g., *Milton*, 2002]. In subsurface hydrology, the need to define an effective hydraulic-conductivity tensor has been recognized since the pioneering work of *Theis* [1935] and has successively been the topic of a large body of specific literature, well summarized in a few comprehensive reviews [e.g., *Sanchez-Vila et al.*, 1995; *Renard and de Marsily*, 1997; *Neuman and Di Federico*, 2003; *Dagan et al.*, 2013].

A common simplified model of heterogeneous aquifers is derived by computing an effective hydraulic-conductivity tensor, causing the same mean Darcy flow when applying a uniform-in-the-mean hydraulic gradient, as the true heterogeneous conductivity field [e.g., *Paleologos et al.*, 1996; *Renard and de Marsily*,

1997; *Jankovic et al.*, 2003; *Zhou et al.*, 2010]. Effective hydraulic-conductivity tensors can be (i) derived by closed-form upscaling [e.g., *Indelman and Dagan*, 1993], requiring a geostatistical description of the local conductivity field, (ii) computed by renormalization [e.g., *Durlofsky*, 1992], requiring the exact spatial conductivity distribution, or (iii) estimated by fitting models to larger-scale hydraulic observations such as regionally distributed hydraulic-head measurements or pumping-test data [e.g., *Hantush and Thomas*, 1966]. Since the correlation structure of the heterogeneity is typically anisotropic to account for the different spatial extents of characteristic depositional units in sedimentary aquifers [e.g., *Mial*, 1996], effective hydraulic-conductivity tensors are mostly anisotropic, even if the underlying fully resolved conductivity field was generally assumed stationary and locally isotropic.

Natural sediments may show anisotropy on all scales, including the local Darcy scale. However, local anisotropy of porous formations has been commonly considered of secondary importance in comparison to heterogeneity, which is considered the most salient feature of hydrogeology [*Sanchez-Vila et al.*, 2006]. At the pore scale, particles with irregular shape, such as the plate-shaped particles of mica, are generally oriented with the flat side down [see *Kim et al.*, 1987, Figure 8], thus resulting in larger conductivity in the direction of the bedding plane than perpendicular to it [*Bear*, 1972]. Local anisotropy may remain undetected when estimates of hydraulic conductivity are obtained from inversion of experimental data (e.g., from pumping tests) under the implicit assumption of isotropy and at a scale that does not allow the identification of fine-scale sedimentary structures, and when hydraulic conductivity estimates are based on grain-size analysis [e.g., *Alyamani and Sen*, 1993] and slug tests [e.g., *Bouwer and Rice*, 1976], which also cannot capture the effect of anisotropy.

Sedimentation processes may determine the anisotropic nature of the hydraulic conductivity tensor [e.g., *Friedman and Seaton*, 1996; *Hsieh et al.*, 1985]. Graded bedding, leads to sequences of layers, each of them fining up toward the top. In this case, alternating layers with different isotropic texture can be modeled at the formation scale as an anisotropic medium, with higher conductivity values in the directions parallel to the bedding planes than perpendicular to it [*Bear and Dagan*, 1965]. The complexity of the processes controlling aquifers formation leads to complicated structures in which anisotropic and heterogeneous zones can be distinguished [*Blatt et al.*, 1980]. For example, dunes are created by the deposition of inclined layers (cross bedding) with respect to the main depositional direction, which is also the principal direction of the hydraulic-conductivity tensor, thereby generating an anisotropic geological structure. Similarly, braided rivers generate complex patterns of troughs and channels which are filled with tilted sediment layers. Since the direction of deposition changes from one sedimentary structure to the next, the overall result is a locally anisotropic and heterogeneous (spatially variable) hydraulic-conductivity tensor [*Poeter and Gaylord*, 1990; *Heinz et al.*, 2003; *Kostic and Aigner*, 2007; *Sun et al.*, 2008; *Ramanathan et al.*, 2010; *Guin et al.*, 2010]. As a consequence, the tensorial nature of hydraulic conductivity manifests itself with spatially varying orientation and degree of anisotropy, at scales ranging from a few centimeters to several kilometers [e.g., *McLaughlin and Townley*, 1996; *Heinz et al.*, 2003; *Ritzi and Allen-King*, 2007; *Ronayne et al.*, 2010]. In the statistical description of the hydraulic-conductivity field, the spatial variability of anisotropy is expressed as spatial nonstationarity to evidence that geostatistical properties change in space. Figure 1, taken from *Heinz and Aigner* [2003], illustrates some of the mentioned features occurring in real aquifers and points toward investigation techniques appropriate for the scale of interest of the different geological structures.

While the impact of upscaling isotropic stationary heterogeneous fields has been investigated at depth for macrodispersion [for reviews, see *Dagan*, 1989; *Gelhar*, 1993; *Rubin*, 2003], including some limitations in reproducing experimental and numerical results [e.g., *Battiato et al.*, 2011; *Chiogna and Bellin*, 2013], the effect of upscaling on flow topology has received little attention. In fact, only a few studies have focused on flow topology in porous media [e.g., *Bear*, 1972; *Sposito*, 1994, 2001; *de Barros et al.*, 2012]. Topological metrics can be used to identify flow patterns causing plume deformations with relevant effects on transverse solute fluxes, thereby enhancing mixing, as evidenced by *de Barros et al.* [2012] for two-dimensional stationary flow fields, and with potential innovative applications in engineered remediation systems, as shown in a few studies conducted in two-dimensional transient flow fields [*Neupauer et al.*, 2014; *Piscopo et al.*, 2013; *Weeks and Sposito*, 1998; *Bagtzoglou and Oates*, 2007].

Topology of steady-state three-dimensional flow fields has been described, for example, by *Sposito and Weeks* [1998] and *Sposito* [2001] for isotropic heterogeneous formations. Anisotropic media has been recently investigated by *Chiogna et al.* [2014], although already the studies of *Bakker and Hemker* [2002, 2004], *Hemker and Bakker* [2006], and *Hemker et al.* [2004] pointed out that anisotropy in some cases may lead to velocity fields
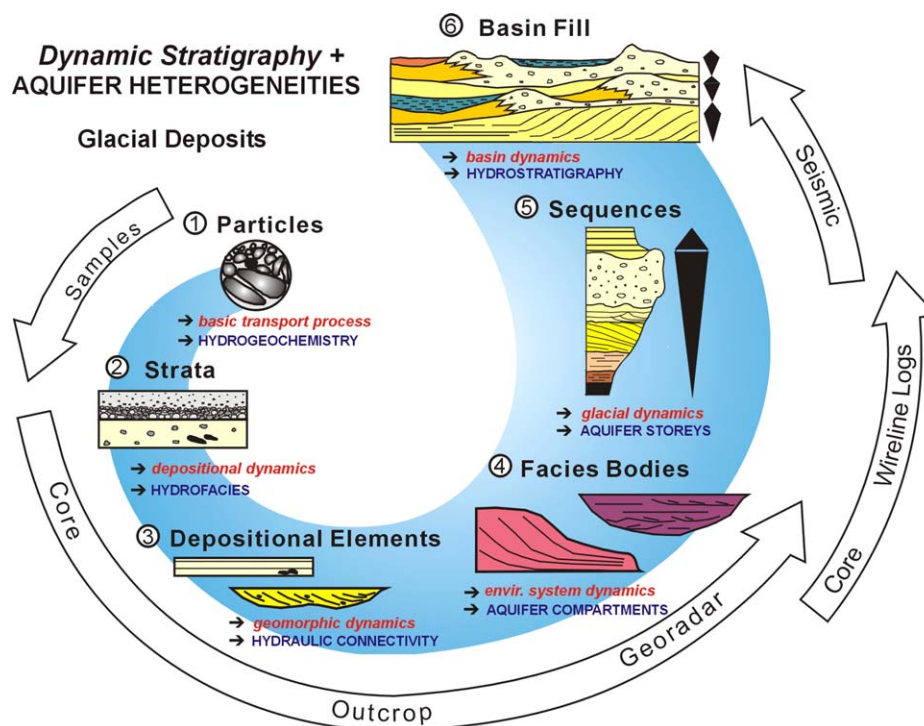
Figure 1. Sedimentological structures occurring at different scales in natural aquifers [taken from *Heinz and Aigner*, 2003].

with large-scale periodic structures. In particular, the occurrence of groundwater whirls was demonstrated by Bakker and coworkers for blockwise uniform locally anisotropic porous media where the orientation of anisotropy differed from block to block. In addition, *Stauffer* [2007] investigated the impact of highly permeable sediment units with inclined bedding on the occurrence of groundwater whirls.

Differently from previous contributions, in this work we focus our attention on steady-state three-dimensional groundwater flow in a nonstationary heterogeneous porous medium with the hydraulic conductivity that is locally isotropic at the Darcy scale, but that becomes anisotropic when upscaled to a larger scale by defining homogeneous equivalent hydraulic conductivity blocks. The resulting features of complex flow topology and the implications for mixing are analyzed using the helicity density as well as two kinematic descriptors of mixing: stretching and folding. The helicity density is an important descriptor of flow topology [*Arnold and Khesin*, 1998; *Moffatt and Tsinober*, 1992; *Sposito*, 2001], it is defined as the scalar product of the velocity vector and its curl and its correct computation is a benchmark for numerical solution of flow equations [*Liu and Wang*, 2004]. The helicity density is a point-scale property of the velocity field; therefore, its value depends on the scale at which the velocity field is resolved. Hence, currently available upscaling strategies may not preserve the topological characteristics of the original flow field. Furthermore, we analyze large-scale patterns of the streamlines deformation by computing stretching and folding, two metrics proposed by *Falk and Langer* [1998] and *Kelley and Ouellette* [2011] in studying mixing properties of transient turbulent flow fields, which allow to separate linear (stretching) from nonlinear (folding) deformation mechanisms, both reflecting large-scale patterns of the flow field with relevant implications on mixing. It can be shown, in fact, that stretching and folding measure the affine and nonaffine components of the plume deformation [*Kelley and Ouellette*, 2011] at different scales and provide useful information on mixing potential of the flow field, separating deformation mechanisms caused by the occurrence of scale-dependent flow structures.

Specific objectives of the present study are to: (i) show how simple nonstationarity in the hydraulic conductivity distribution may influence large-scale structures of the velocity field in a heterogeneous formation; (ii) illustrate how the numerical artifacts introduced in numerical simulations with relatively large computational cells and upscaling of the flow equation may influence the topology of the flow field; and (iii) apply stretching and folding as kinematic metrics to distinguish between the different contributions on mixing enhancement caused by the deformation of plume material surfaces due to the influence of flow

heterogeneity and of flow topology (i.e., twisting streamlines). In the companion paper *Cirpka et al.* [2015], we explicitly address the solute-transport problem and show how the scale dependence of the flow topology and the kinematic descriptors analyzed in this work are related to plume dilution and in particular to entropy-based metrics of the distribution of solute concentration [e.g., *Kitanidis*, 1994; *Rolle et al.*, 2009].

2. Helicity Density and Metrics of Stream-Tube Deformation in Porous Media

Flow in porous media is described by Darcy's law:

$$\mathbf{q}(\mathbf{x}) = -\mathbf{K}(\mathbf{x})\nabla\phi(\mathbf{x}) \tag{1}$$

where $\mathbf{q}(\mathbf{x})[LT^{-1}]$ is the vector of specific discharge, $\mathbf{K}(\mathbf{x})[LT^{-1}]$ is the hydraulic-conductivity tensor, and $\phi(\mathbf{x})[L]$ is the hydraulic head. Substituting equation (1) into the continuity equation for the case of zero sources and sinks, $\nabla \cdot \mathbf{q} = 0$, results in the groundwater-flow equation:

$$\nabla \cdot (\mathbf{K}\nabla\phi) = 0 \tag{2}$$

The spatial integral of the helicity density of the flow field $h[LT^{-2}]$ is a topological invariant [*Moffatt and Tsinober*, 1992], which quantifies how streamlines twist around an axis aligned with the direction of flow, resulting into helical curves in three-dimensional space [*Sposito*, 2001]. The helicity density is defined as the scalar product of the specific-discharge vector $\mathbf{q}(\mathbf{x})$ and the vorticity (i.e., the curl of the specific discharge $\mathbf{w}(\mathbf{x}) = \nabla\times\mathbf{q}(\mathbf{x})$ [*Kapoor*, 1997]):

$$h(\mathbf{x}) = \mathbf{q}(\mathbf{x}) \cdot (\nabla\times\mathbf{q}(\mathbf{x})) \tag{3}$$

In addition, the relative helicity density $h_r(\mathbf{x})[-]$ can be defined as follows:

$$h_r(\mathbf{x}) = \frac{\mathbf{q}(\mathbf{x}) \cdot (\nabla\times\mathbf{q}(\mathbf{x}))}{||\mathbf{q}(\mathbf{x})||_2 ||\nabla\times\mathbf{q}(\mathbf{x})||_2} \tag{4}$$

which is the cosine of the angle between $\mathbf{q}$ and its curl $\nabla\times\mathbf{q}$. In equation (4), $||\cdot||_2$ is the L_2 norm.

The helicity density can be computed by substituting equation (1) into equation (3). A detailed analysis on the sufficient and necessary conditions to obtain a velocity field with nonvanishing helicity density in porous media has been provided by *Chiogna et al.* [2014]. While helicity density can be used to identify the occurrence of important structures, such as groundwater whirls [*Hemker et al.*, 2004; *Bakker and Hemker*, 2004; *Hemker and Bakker*, 2006], flow fields showing zero local helicity density may still exhibit other types of deformations induced by rotation associated with vorticity, also relevant to mixing processes, such as stretching and folding. These are large-scale metrics of plume deformation directly related to streamline geometry [e.g., *Kelley and Ouellette*, 2011]. Mixing, in fact, is intimately related to the deformation of the plume because local diffusive/dispersive fluxes depend on local dispersion and concentration gradients, which are strongly affected by stretching and folding [e.g., *Ottino*, 1989; *de Barros et al.*, 2012].

We propose to apply descriptors of deformation to groundwater plumes that have been used to capture the dynamics of viscoplastic deformation in amorphous solids [*Falk and Langer*, 1998]. In steady-state flow, the deformation of streamtubes can be analyzed within the x_2, x_3-plane while moving along the x_1-direction. As illustrated in Figure 2, we consider a set of N streamlines surrounding a central reference streamline. The distance of the central streamline from one of the surrounding streamlines forming the cluster is given by:

$$\mathbf{d}^n(x_1) = \mathbf{x}^0(x_1) - \mathbf{x}^n(x_1) \tag{5}$$

in which n is the index of the streamline, and $\mathbf{x}^n(x_1)$ is the vector of two coordinates, which identifies the point at which the streamline crosses the plane x_1. At $x_1 = 0$, the set of N streamlines form a circle with the initial distance r_0 from the central streamline (see Figure 2):

$$d_2^n(0) = r_0\cos(2\pi n/N)$$
$$d_3^n(0) = r_0\sin(2\pi n/N) \tag{6}$$

The deformation, along the direction x_1, of the circle defined by equation (6), is given by the dynamic behavior of the vectors $\mathbf{d}^n(x_1 + \Delta x_1)$, describing how the shape of the streamtube changes
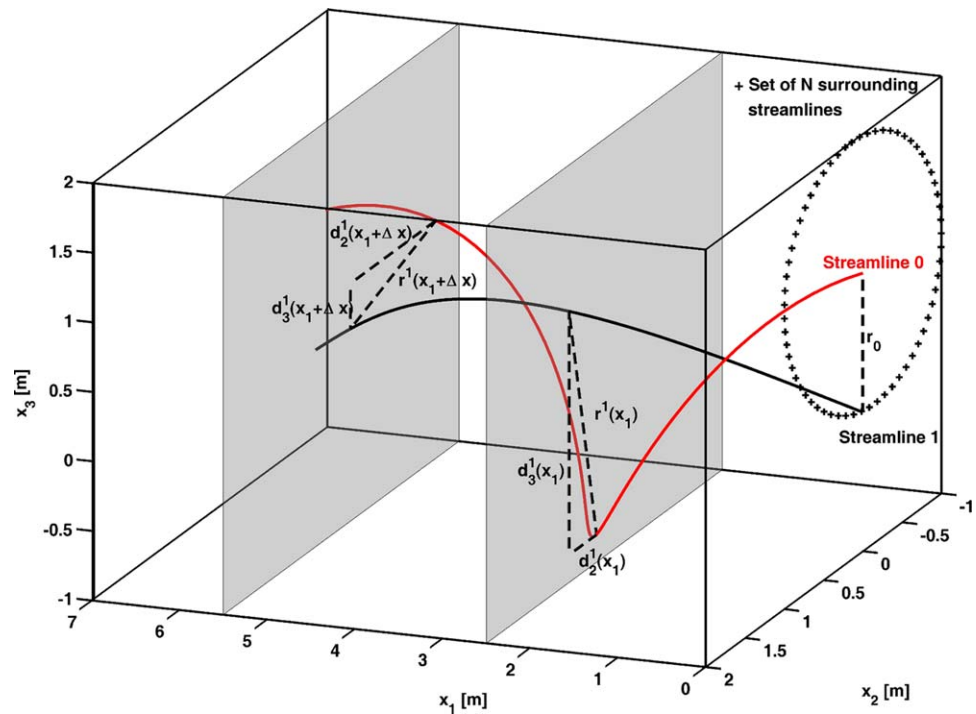
Figure 2. Streamlines evolution in the main flow direction x_1 tracked with a set of N particles, displaced in circle of radius r_0 at the inlet boundary. The solid red and black lines are the traces of two representative streamlines, and the dashed lines illustrate the procedure to calculate their relative distance at different cross sections.

when moving from the plane x_1 to the plane $x_1 + \Delta x_1$. The space interval Δx_1, therefore, is the analogous of the deformation time used by *Kelley and Ouellette* [2011]. The affine component of the deformation can be identified by least square fitting the following linear model to the deformation of the streamlines [*Falk and Langer*, 1998]:

$$\mathbf{d}_{aff}^n(x_1 + \Delta x_1) = (\mathbf{A} + \mathbf{I})\mathbf{d}^n(x_1) \tag{7}$$

in which the affine deformation matrix $\mathbf{A}$ is identical for all streamlines n, but may differ from one increment $[x_1, x_1 + \Delta x_1]$ to the next, and $\mathbf{I}$ is the identity matrix. The affine deformation matrix $\mathbf{A}$ can be written as follows [*Falk and Langer*, 1998]:

$$\mathbf{A} = \mathbf{W}\mathbf{J}^{-1} - \mathbf{I} \tag{8}$$

where the two matrices $\mathbf{W}$ and $\mathbf{J}$ are given by:

$$\mathbf{W} = \sum_{n=1}^{N} \mathbf{d}^n(x_1) \otimes \mathbf{d}^n(x_1 + \Delta x_1) \tag{9}$$

and

$$\mathbf{J} = \sum_{n=1}^{N} \mathbf{d}^n(x_1) \otimes \mathbf{d}^n(x_1), \tag{10}$$

respectively. In equations (9) and (10), $\otimes$ denotes the matrix product.

Stretching is thus defined as the normalized L_2-norm squared of the affine deformation of the streamlines:

$$A^2(\mathbf{x}, \Delta x_1) = \frac{1}{r_0^2 N} \sum_{n=1}^{N} ||\mathbf{A}\mathbf{d}^n(x_1)||_2^2 \tag{11}$$

and folding is defined similarly as the normalized L_2-norm squared of the nonaffine (nonlinear) part of the overall deformation:

$$D^2(\mathbf{x}, \Delta x_1) = \frac{1}{r_0^2 N} \sum_{n=1}^{N} ||\mathbf{d}^n(x_1 + \Delta x_1) - (\mathbf{A}+\mathbf{I})\mathbf{d}^n(x_1)||_2^2 \tag{12}$$

Folding, therefore, represents the inability of describing the deformation with a purely linear model. From a physical point of view, stretching represents the increase of the length of an interface, while folding describes how this interface is bent in order to fill a finite volume of space [*Kelley and Ouellette*, 2011].

3. Anisotropy Resulting From Upscaling in Heterogeneous Porous Media

As we recalled in section 2, local properties of the conductivity field, in particular anisotropy, are the main controlling factors determining the topological characteristics of the flow field [*Bear*, 1972]. In a heterogeneous formation, the spatial variability of hydraulic properties is typically described by assuming that the logarithm of the hydraulic conductivity, $Y(\mathbf{x}) = \ln K(\mathbf{x})$, is a statistically second-order stationary random space function with constant mean $\langle Y \rangle$, variance σ_Y^2, and a given two-point correlation function. According to these assumptions, the spatial distribution of the hydraulic conductivity can be written as follows:

$$K(\mathbf{x}) = e^{Y(\mathbf{x})} = K_G e^{Y'(\mathbf{x})} \tag{13}$$

where $K_G = \exp[\langle Y \rangle]$ is the geometric mean of hydraulic conductivity and $Y'(\mathbf{x})$ is the fluctuation about the mean. The description of the random space function is completed with the choice of the two-point covariance function, which describes the spatial correlation of the log conductivity field. One of the most used models of spatial variability is the Gaussian covariance model:

$$C_Y(r') = \sigma_Y^2 \exp[-r'2] \tag{14}$$

where $r' = \sqrt{(r_1/\lambda_1)^2 + (r_2/\lambda_2)^2 + (r_3/\lambda_3)^2}$, with λ_1, λ_2, and λ_3 being the correlation lengths in the principal directions x_1, x_2, and x_3, respectively, which are assumed to be aligned with the Cartesian reference system, and $r_i = x'_i - x_i$, $i = 1, 2, 3$ are the components of the two-point separation distance [e.g., *Dagan*, 1989]. This model of spatial variability, which is commonly adopted in modeling studies dealing with heterogeneous formations, implicitly assumes that the hydraulic conductivity is locally isotropic, i.e., the hydraulic conductivity is a scalar quantity, though it varies in space according to the adopted model of spatial variability.

Alternatively, to take advantage of the large library of solutions available for homogeneous conductivity fields, a suitable effective hydraulic-conductivity tensor may be defined [e.g., *Wen and Gomez-Hernandez*, 1996; *Renard and de Marsily*, 1997; *Dagan et al.*, 2013]. The methods used to define the effective hydraulic conductivity include small-perturbation analysis, the self-consistent approximation, and methods that impose to match the energy dissipation of the actual and effective conductivity fields [e.g., *Sanchez-Vila et al.*, 1995; *Renard and de Marsily*, 1997; *Neuman and Di Federico*, 2003; *Dagan et al.*, 2013; *Jankovic et al.*, 2013]. Whatever technique is used, the effective hydraulic conductivity is mostly anisotropic, even when the original heterogeneous field is locally isotropic, i.e., $K_{eff,11} \neq K_{eff,22} \neq K_{eff,33}$. $\mathbf{K}_{eff}$ may also include nonzero off-diagonal terms. A similar conclusion can be reached for the upscaled equivalent block-effective hydraulic conductivity at the scale of the computational cells [e.g., *Zhou et al.*, 2010]. Indeed, an equivalent hydraulic conductivity tensor can be defined also by upscaling the hydraulic conductivity to the computational cells in numerical models. In this case, the fine-scale continuous hydraulic-conductivity field is replaced with an equivalent distribution of hydraulic conductivity, which varies stepwise within the domain. The effect of the commonly adopted upscaling techniques has been analyzed by *Cainelli et al.* [2012], among others.

In the present study, we consider the first-order approximation in σ_Y^2 obtained by *Gelhar and Axness* [1983] for a three-dimensional anisotropic (i.e., $\lambda_1 \neq \lambda_2 \neq \lambda_3$) conductivity field:

$$K_{eff,ii} = K_G J_i \left[\left(1 + \frac{\sigma_Y^2}{2}\right) - \alpha_i \right] \tag{15}$$

with

$$\alpha_i = \frac{1}{(2\pi)^{3/2}} \int_{-\infty}^{\infty} \int_{-\infty}^{\infty} \int_{-\infty}^{\infty} \frac{\mathbf{J} \cdot \mathbf{k} k_i}{k^2} S_Y(\mathbf{k}) d^3\mathbf{k} \tag{16}$$

where $\mathbf{J}$ is the vector of the mean hydraulic gradient, $\mathbf{k} = (k_1, k_2, k_3)$ is the frequency variable in the Fourier space, $k^2 = k_1^2 + k_2^2 + k_3^2$, $d^3\mathbf{k} = dk_1 dk_2 dk_3$, and S_Y is the spectral density function of the log conductivity
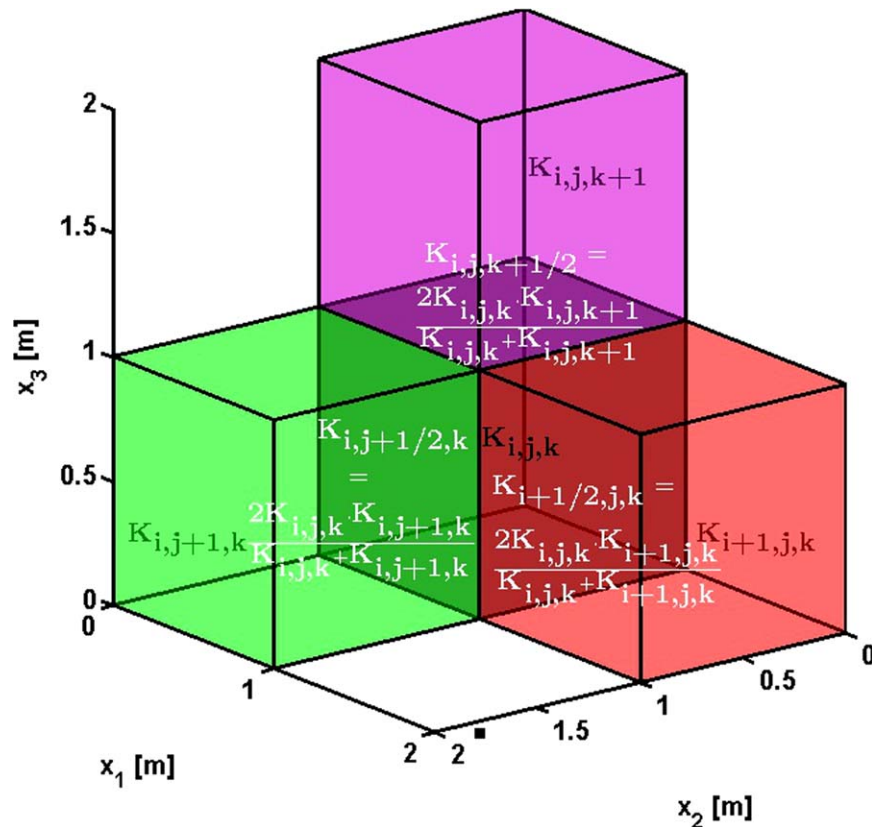
Figure 3. Example of numerical discretization of the 3-D domain and computation of the hydraulic conductivity at different cell interfaces.

covariance function, which for the Gaussian covariance model of equation (14) assumes the following expression [*Rubin*, 2003, equation 2.50c]:

$$S_Y(\mathbf{k}) = \frac{1}{\sqrt{8}} \sigma_Y^2 \lambda_1 \lambda_2 \lambda_3 \exp\left[-\sum_{j=1}^{3} k_j^2 \lambda_j^2 / 4 \right] \tag{17}$$

Equation (15) takes implicitly into account that the effective conductivity tensor is diagonal, such that $K_{eff,ij} = 0$ for $i \neq j$ [*Dagan*, 1989, p. 192].

4. Artificial Anisotropy Caused by the Numerical Solution of the Flow Problem

In a heterogeneous formation, the flow equation (2) is generally solved numerically with grid dimensions of only a fraction of the correlation lengths, such as to minimize the error caused by neglecting subgrid-scale variability [e.g., *Li et al.*, 2010; *Herrera et al.*, 2010; *Cainelli et al.*, 2012]. As in most numerical applications, we consider in the present work a fine discretization and assign to a given cell a uniform and isotropic hydraulic-conductivity value obtained by sampling the random *K*-field with spacing equal to the grid dimensions. The flow equation (2) is discretized by the cell-centered Finite Volume Method with regular grid spacing, taking the harmonic average of the hydraulic conductivities of two adjacent cells as the effective conductivity for the interface shared by the cells.

In order to obtain a good reproduction of the conductivity field, a grid spacing as small as $\delta x_i = \sqrt{\pi} \lambda_i / 8$, or smaller, should be used [e.g., *Bellin et al.*, 1992; *Cainelli et al.*, 2012]. While in two-dimensional applications finer grid resolutions are often used, such fine spacing is computationally challenging in most three-dimensional studies.

Since the discrete fluxes between adjacent cells are computed by using a suitable average of the hydraulic-conductivity values of the two cells, the conductivities applied in the different directions differ, unless the
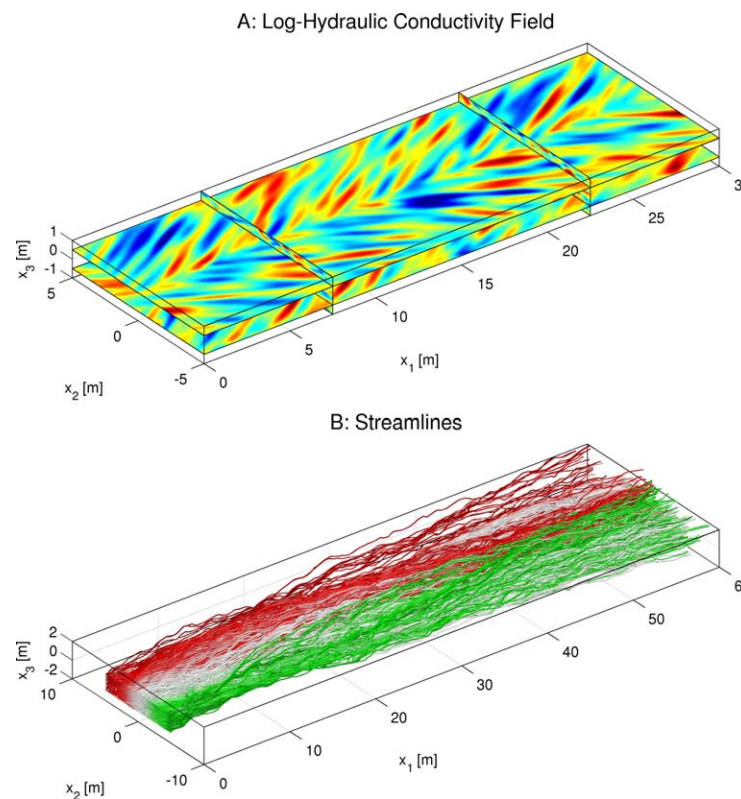
hydraulic conductivities of the central cell and its six neighbors are identical (the sketch of the spatial arrangement of the computational blocks is shown in Figure 3). That is, the numerical scheme causes artificial anisotropy even when the underlying discretized conductivity field is locally isotropic. As shown by *Cainelli et al*. [2012], this numerical artifact is reduced when flow is solved by the Galerkin Finite Elements scheme, or the Finite Volume Method with the harmonic mean replaced by the arithmetic mean, but to make it negligible a grid spacing as small as $\delta x_i = 0.05 \lambda_i$ and $\delta x_i = 0.1 \sqrt{\pi} \lambda_i / 2$ for the exponential and Gaussian covariance function, respectively, or smaller should be used.

Therefore, a finer discretization than that required by the Nyquist theorem, which needs at least two sampling points per integral scale in order to reproduce correctly the random fluctuations of the conductivity field, should be used to minimize the alteration of local flow topology introduced by the tensor of effective hydraulic conductivity.

In an attempt to alleviate this problem, *Li et al*. [2010] developed a numerical method in which the sampled hydraulic conductivity is directly assigned to the cell interface, instead of the cell center, thereby avoiding the need to define equivalent hydraulic conductivities. However, they showed that this method does not provide advantages in term of accuracy when the tensor of the local hydraulic conductivity is diagonal, but anisotropic, as in the cases considered in the present work.

5. Numerical Results of Flow Topology in Fully Resolved and Upscaled Nonstationary Hydraulic-Conductivity Fields
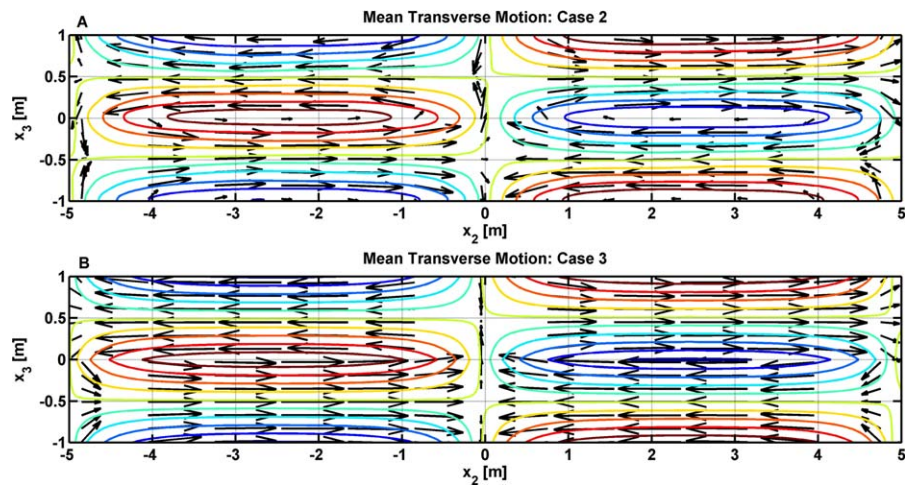
We now consider a three-dimensional heterogeneous log conductivity field with blockwise stationary, periodic, anisotropic Gaussian model of spatial variability, according to equation (14). The log conductivity variance σ_Y^2 is set to 2.0, the three correlation lengths are $\lambda_1 = 2$ m, $\lambda_2 = 0.4$ m, and $\lambda_3 = 0.1$ m, while the geometric mean of hydraulic conductivity is $K_G = 1 \times 10^{-4}$ m/s. The computational domain is composed of four blocks 5 m wide, 1 m high, and 30 m long, arranged in two layers with the longer dimension oriented along the mean flow direction x_1 and the lateral surfaces joined to obtain a unit cell 30 m long, 10 m wide, and 2 m high, in the x_1, x_2, and x_3-directions, respectively. The top left and bottom right blocks share the same random space function with the primary principal direction rotated by 30° to the left of the x_1-direction. Similarly, the top right and bottom left blocks share the same random space function, which is independent from that of the other two blocks, with the primary principal direction rotated by 30° to the right of the x_1-direction. These two random fields are generated with the spectral approach of *Dietrich and Newsam* [1993]. The

Figure 4. Numerical test Case 1: (a) nonstationary heterogeneous conductivity field and (b) computed streamlines.

Figure 5. (a) Mean transverse motion of the flow field in Case 2 (average of 50 Monte Carlo realizations of Case 1). (b) Mean transverse motion of the flow field in Case 3 (upscaled flow field derived from Case 1).

transition between the blocks is obtained by blending the log conductivity fields using a Tukey window [*Tukey*, 1967] with a transition zone of 1 m in the x_2-direction and 0.2 m in the x_3-direction.

The uniform grid spacing is 0.1 m in the two horizontal directions and 0.02 m in the vertical one, leading to a total of 3×10^6 elements. The number of points per correlation length are therefore 20 in the longitudinal direction, while in the transverse horizontal and vertical directions they are 4 and 5, respectively, which is enough to reproduce the conductivity field [*Bellin et al.*, 1992]. A constant scalar value of hydraulic conductivity is assigned to each computational element by sampling the random fields with the same spacing; the resulting log conductivity field is shown in Figure 4A. Consequently, the numerical artifacts introduced by discretization, particularly the equivalent local anisotropy of the hydraulic-conductivity tensor [*Li et al.*, 2010] and the helicity density discussed in section 4, are expected to be negligible. This will be tested for the numerical solution of the flow field.
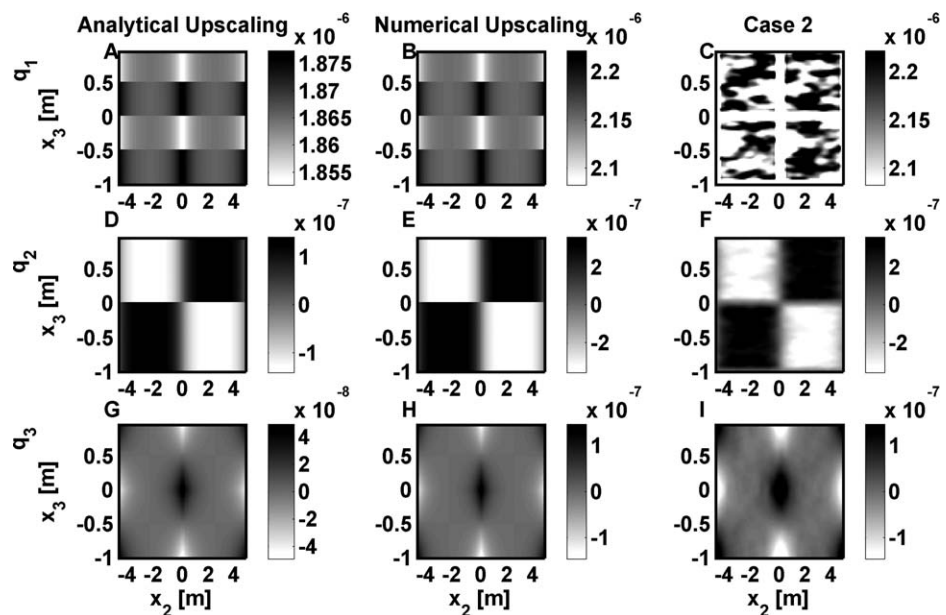

Figure 6. Components of the specific discharge for the case in which the effective conductivity tensor has been computed (a, d, and g) analytically, (b, e, and h) numerically and (c, f, and i) Case 2. The first row shows the longitudinal component, while the transverse horizontal and vertical components are shown in the second and third row, respectively.

Table 1. Summary of the Analyzed Cases

Case	K Field	Velocity Field	Overall Objective	Main Features
1	Heterogeneous, locally isotropic conductivity field with blockwise stationary Gaussian covariance function, equation (14)	Fully resolved	Analysis of flow topology in a heterogeneous fully resolved nonstationary K field	Helicity density is locally zero, stretching and folding influenced by small-scale heterogeneity
2	Not defined	Uniform along x_1 (average along x_1 of the velocity components of 50 realizations of Case 1)	Evidence large-scale helical structures of the Case 1	Helicity density is different from zero, reduced stretching and folding at short distance with respect to Case 1 due to the averaging
3	Blockwise homogeneous anisotropic effective conductivity field	Upscaled flow field of Case 1	Analysis of flow topology in a homogeneous upscaled anisotropic K field	Helicity density is different from zero, reduced stretching and folding with respect to Case 1 due to the homogeneity of the medium

Periodic head conditions with a mean hydraulic gradient of 0.01 are applied to the external surfaces of the computational domain such that the mean flow field is oriented along the x_1-direction. We numerically solve the groundwater flow equation (2) and Darcy's law, equation (1), to obtain a periodic velocity field. Successively, streamlines are constructed by tracking 50,000 particles released at the nodes of a uniform squared grid with spacing of 0.02 m within the inlet plane at $x_1 = 0$ using Pollock's semianalytical method [*Pollock*, 1988] (see Figure 4B). Observation planes are set at intervals of 0.1 m in the x_1-direction. The streamlines are tracked over a distance of 60 m in the x_1-direction, i.e., the length of two unit cells. Because of the periodic boundary conditions and the periodic K-field, the velocity field is infinitely self-repetitive in all directions and streamlines can be tracked through neighboring unit cells.

The streamlines depicted in Figure 4B show a complex arrangement in which, for example, streamlines starting from the left and right boundaries of the inlet plane intertwine. A similar behavior is observed with streamlines originating from the top and the bottom of the inlet plane. Overall, the streamlines are observed to twist, forming macroscopic helical structures. The arrows in Figure 5a visualize the transverse horizontal and vertical components of the mean specific-discharge vector computed averaging over 50 Monte Carlo realizations of the heterogeneous field and along the planes normal to the direction x_1, which are superimposed onto the primary component along the direction x_1. The contour lines are streamlines constructed from the mean velocity components in the x_2 and x_3-directions. Altogether, the nonstationary spatial anisotropy of the covariance function
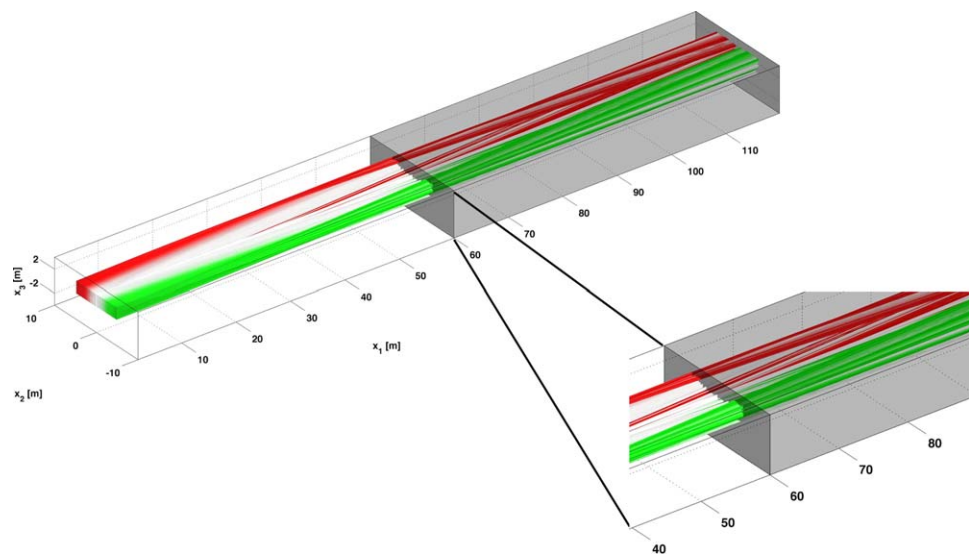
Figure 7. Computed streamlines for Case 3. The shaded region is an extension of the domain used to illustrate that streamlines intertwining is occurring at longer distances than in Case 1. The zoom-in highlights the region where complete twisting of the streamlines occurs.
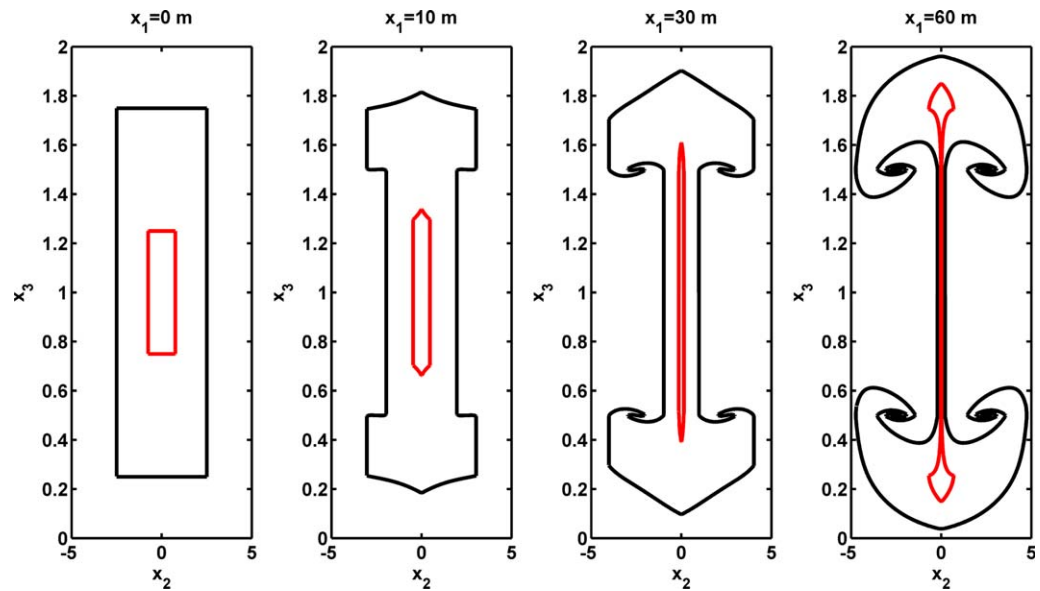
Figure 8. Deformation of two rectangles with different dimensions in the flow field of Case 3 at different distances from the source.

causes significant secondary motion, despite the hydraulic-conductivity field being locally isotropic. Both the primary and secondary motion are perturbed by small-scale variation in the x_1-direction.

In the present work, we compare three different flow fields. The flow field discussed so far, hereafter indicated as Case 1, is numerically computed using the fully resolved locally isotropic hydraulic-conductivity field with a nonstationary anisotropic covariance function of the log conductivity perturbations. To complete the analysis, we consider two upscaled cases derived from this base case. In Case 2, the velocity field of Case 1 is averaged along the x_1-direction and through the 50 Monte Carlo realizations to obtain a new velocity field, which is uniform along x_1 but variable in the other two directions. Finally, in Case 3, the flow field is computed using a blockwise homogeneous anisotropic effective conductivity tensor. The components of the effective conductivity tensor have been computed according to the following two approaches. In the first approach, an effective conductivity is computed by substituting the statistical parameters of the stationary conductivity field used as base for the Case 1 into equation (15); the resulting diagonal tensor is then modified by rotation, to align its principal direction with the two blockwise principal directions of heterogeneity in Case 1 (the integral of equation (16) is solved numerically). The second approach differs from the first one only in the way the effective conductivity is computed: instead of using equation (15) the effective conductivity is computed numerically by dividing the mean flow by the mean head gradient. Figure 6 compares the three components of the specific discharge obtained computing the values of the effective hydraulic conductivity analytically (Figures 6a, 6d, and 6g) and numerically (Figures 6b, 6e, and 6h). The comparison is also extended to the mean flow field of Case 2 (Figures 6c, 6f, and 6i). The most interesting components are those in the x_2 and x_3-directions, reproduced in the subplots of the second and third row, respectively, since they are responsible for the secondary motion. Inspection of the figure reveals that these transverse components are very similar for the three cases considered. The x_1-component of Case 2 (see Figure 6d) still shows some irregular patterns, indicating that more realizations would be needed to obtain the correct effective velocity field also in that direction, although the mean value and the range of variability of the three cases are comparable. Furthermore, Case 2 displays less sharper transition zones than the other two cases between velocity components in the different blocks due to the use of the Tukey window function for the generation of the conductivity fields. The velocity field obtained using the effective conductivity tensor computed analytically and numerically are both in good agreement with Case 2, however, the latter are to be preferred since the magnitude of the three components of the flow field are more similar to Case 2. Therefore, in the following, Case 3 will refer to the results obtained using the effective conductivity tensor computed taking advantage of the set of Monte Carlo realizations. Table 1 summarizes the three cases.

Cases 1 and 2 are constructed in such a way that a mean secondary motion is generated with periodic recurrence of two circulation cells, one rotating clockwise and the other counterclockwise in the plane

x_2-x_3 as shown in Figure 5a. No flow crosses the vertical planes normal to the x_2-direction at $x_2=-5$m, 0 and 5 m, and the horizontal planes at $x_3=-0.5$m and 0.5 m.

A similar mean flow field is obtained in Case 3 where a uniform, but anisotropic hydraulic conductivity tensor is assigned to the four blocks forming the computational domain, as shown in Figure 5b. In this case, the flow field is obtained analytically using the method of *Bakker and Hemker* [2004]. The corresponding streamlines, obtained by injecting the particles in the same grid nodes as in Case 1 are shown in Figure 7. Since the hydraulic conductivity is homogeneous within the blocks, the resulting streamlines are smoother than in the heterogeneous Case 1. However, they exhibit a large-scale helical structure, which deforms solute plumes. In particular, streamlines originating in the left portion of the inlet plane (colored in red) spiral clockwise while they tilt to the right and those originating from the right portion of the inlet plane (colored in green) spiral clockwise while they tilt to the left.

Figure 8 illustrates for Case 3 the deformation that two closed rectangular lines starting in the vertical plane x_2-x_3 at $x_1=0$ experience upon transport along the direction x_1. We can observe that, even if the medium is blockwise homogeneous, the deformation processes are significantly different for the inner (red) and outer (black) rectangles. In particular, the inner rectangle is just stretched in the vertical x_3 direction up to a distance of 60 m, while the black rectangle is stretched also in the transverse x_2 direction and at a distance of 60 m folding is evident due to the generation of four spiral arms.

5.1. Helicity Analysis

According to equation (3), the helicity density depends on the magnitude and orientation of the flow field and of the vorticity field. As shown in Figure 6, the three components of the flow fields of Cases 2 and 3 are characterized by similar and locally rather regular patterns, generating the secondary motion observed in Figure 5, while the fully resolved heterogeneous Case 1 is characterized by flow focusing in high-conductivity zones [e.g., *Werth et al.*, 2006; *Chiogna et al.*, 2011b], whose imprint is evident in the irregular pattern of the streamlines shown in Figure 4. At a first glance, the helical structures observed in the fully resolved flow field of Case 1 are difficult to interpret, since the scalar product between the specific-discharge vector and the vorticity vector is zero [e.g., *Kapoor*, 1997]. So, it is worth to investigate in more details the topology of Case 1 in order to explain the helical structures observed in Figure 4.

The analysis of the rotational properties of the flow field, computing its vorticity, is widely used in fluid mechanics [see e.g., *Ottino*, 1989]. We compare the numerical standard deviations of the three vorticity components, to the first-order analytical expressions of *Kapoor* [1997] for the Gaussian stationary covariance function given by equation (14), and considering that the anisotropic covariance function is rotated by $\pm$ 30° with respect to the mean hydraulic gradient:

$$\sigma_{w_1}=0$$
$$\sigma_{w_2}=\frac{K_gJ\sqrt{2}\sigma_Y}{\lambda_3}$$
$$\sigma_{w_3}=K_gJ\sigma_Y\sqrt{\frac{1}{2\lambda_1^2}+\frac{3}{2\lambda_2^2}}$$

(18)

With the statistical parameters used in the simulations of Case 1, the theoretical (first-order) standard deviations of the vorticity components assume the following values: $\sigma_{w_2}=2\times10^{-5}s^{-1}$ and $\sigma_{w_3}=4.4\times10^{-6}s^{-1}$.

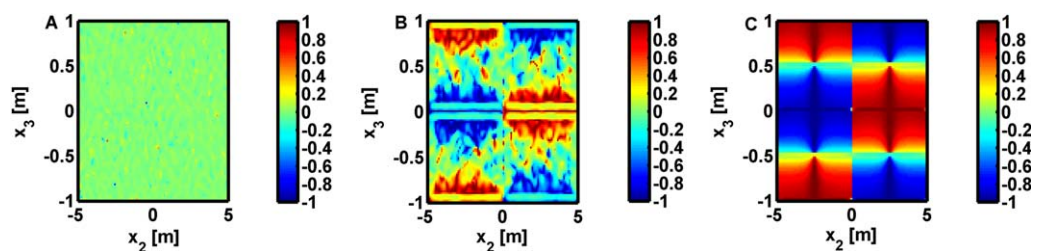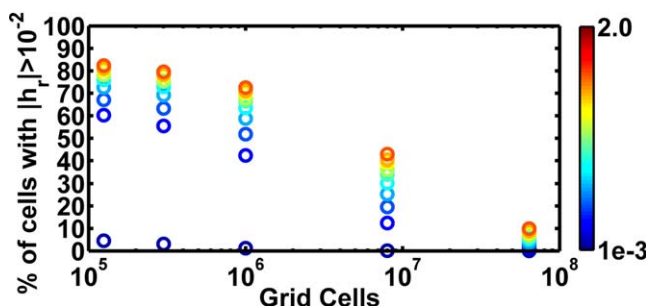**Figure 9.** Relative helicity density as defined in equation (4) computed for a x_2, x_3- cross section at $x_1=10$m, for (a) Case 1, (b) Case 2, and (c) Case 3.

Figure 10. Effect of domain discretization on the absolute value of the relative helicity density. The results are reported for the fully resolved velocity fields (Case 1) and the dependency on σ_Y^2 is illustrated by the color code.

The corresponding numerical estimates for the vorticity are $S_{w_2} = 6 \times 10^{-5} s^{-1}$ and $S_{w_3} = 1.5 \times 10^{-5} s^{-1}$, which are about three times larger. This difference may be attributed to the linear approximation of the closed-form solutions, which formally are valid for $\sigma_Y^2 \ll 1$. In fact, a better agreement with the results of *Kapoor* [1997] is obtained after reducing σ_Y^2 to 0.5. However, the ratio between the standard deviations of w_2 and w_3 is for both log conductivity variances close to the theoretical first-order value, which according to equations (18) is independent of σ_Y^2. The observed largest difference between numerical simulations and theoretical results is for the standard deviation of the longitudinal component of the vorticity, which is zero in the first-order approximation (equation (18)), but in the numerical simulations it equals $S_{w_1} = 1.8 \times 10^{-5}$ s^{-1} for $\sigma_Y^2 = 2$ and therefore comparable to the values obtained for the other two directions (this result was verified also for the case in which $\sigma_Y^2 = 0.5$). We argue that this difference is mainly the consequence of nonstationarity in the covariance function which is responsible for the macroscopic helical structures observed in Case 1, although the validity of the first-order approximation, implying zero uncertainty in the longitudinal component of the vorticity vector, is limited to $\sigma_Y^2 \ll 1$.

Figures 9a–9c show the relative helicity density, as defined by equation (4), for the three cases at the same cross section at $x_1 = 10$m. This quantity is expected to be zero everywhere within the domain with a heterogeneous, but locally isotropic conductivity field such as that used in Case 1. As shown in Figure 9a, and differently from what expected, helicity density in Case 1 is different from zero in some isolated points of the domain. However, its rather small absolute value and the lack of patterns suggest that this residual helicity is the consequence of numerical artifacts and, in particular, of the anisotropy of the equivalent hydraulic conductivity introduced by the numerical scheme used to solve equation (2). To verify this, the simulation was repeated varying the number of grid nodes by almost three orders of magnitude, up to 64×10^6 computational cells, corresponding to 401 grid nodes in each direction. Also the log conductivity variances were varied ranging from 1×10^{-3} to 2 with increments of 0.2. The results of these simulations are summarized in Figure 10, which shows the percentage of computational cells with an absolute value of the relative helicity-density larger than 10^{-2}. The number of computational cells with $|h_r| > 10^{-2}$ reduces by a power law with the number of grid cells, and for a given grid size it declines with decreasing σ_Y^2. This confirms previous studies showing that a higher value of σ_Y^2 calls for a finer numerical discretization. We thus conjecture
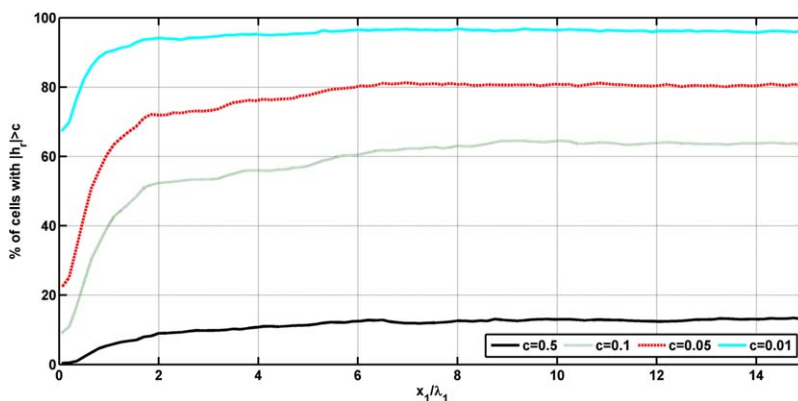
Figure 11. Scale effect on relative helicity density: relative occurrence of its absolute value considering different thresholds c (0.5, 0.1, 0.05, 0.01, black continuous line, green dotted line, red dashed line, and cyan continuous line, respectively) as a function of the averaging length ξ_1 of the flow field of Case 1.
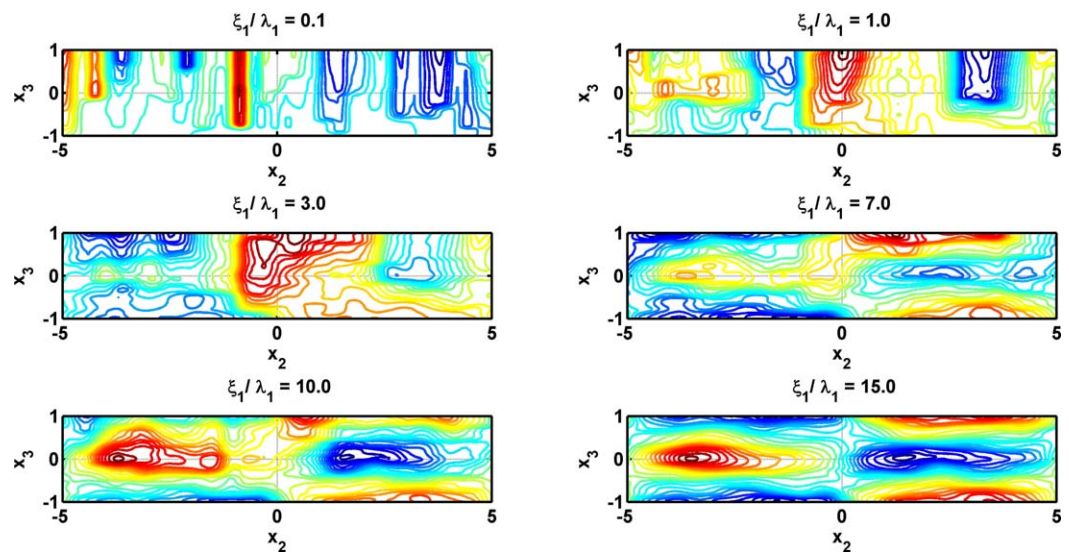
Figure 12. Scale effect on secondary motion: development of secondary motion for different averaging length ξ_1 of the flow field of Case 1.

that the residual relative helicity density observed in Figure 9a is due to spurious small anisotropies introduced by the numerical scheme, which vanish with a sufficiently refined grid.

On the contrary, in the upscaled Case 2, the relative helicity density varies in space spanning the entire range of variability (i.e., between −1 and 1, Figure 9b), with the extreme values obtained when the specific-discharge and the vorticity vectors are parallel. A wide area with nonzero helicity can also be observed in Case 3, as shown in Figure 9c. Positive helicity density values correspond to clockwise helical motion in a right-handed Cartesian coordinate system, while negative helicity density values correspond to counter-clockwise helical motion. The immediate consequence of these observations is that averaging the fully resolved heterogeneous flow field with zero helicity density of Case 1, either by directly averaging $\mathbf{q}(\mathbf{x})$ along the x_1-direction, as done in Case 2, or by applying a blockwise effective uniform anisotropic conductivity tensor, as done in Case 3, does not preserve flow topology. In the two upscaled fields, large-scale helical structures as the ones observed in the original fully resolved field are preserved by the introduction of a local helicity density, not present in the fully resolved field. We argue that streamlines are a scale-dependent concept, so that the possible occurrence of helical structures has to be analyzed at the scale of interest. At the field scale, the model of spatial variability is anisotropic, hence, it is possible to obtain flow fields characterized by nonzero helicity and complex topology on larger scales, although the hydraulic conductivity is parameterized as an isotropic scalar function at the local scale. We denote this as the helicity paradox of flow in nonstationary, statistically anisotropic heterogeneous media.

Figure 11 shows the percentage of cells with the absolute value of relative helicity density larger than a given threshold c, i.e., $|h_r| > c$, in a velocity field obtained by averaging Case 1 in the longitudinal x_1 direction from $x_1 = 0$ to $x_1 = \xi_1$. The computation is performed for several values of the threshold c, considering that values of $c < 0.1$ indicate that the specific-discharge and the vorticity vectors are almost perpendicular. At small ξ_1, the number of cells exceeding the threshold is low, yet nonzero due to the numerical artifacts that we have already discussed. The percentage of cells exceeding the threshold increases with ξ_1 as the anisotropy of the upscaled field increases to flatten for $\xi_1 > 5\lambda_1$. This supports the conclusion that the helicity density is a scale-dependent metric, which should be quantified at the scale of interest to correctly characterize the topology of the flow field. In particular, the analysis of the helicity density is informative on the scale at which helical structures can be expected: at scales lower than one correlation length the helicity density must approach zero in locally isotropic porous media. On the contrary, if we are interested in field-scale processes at spatial scales larger than several correlation lengths we have to consider the flow field at the appropriate scale of interest, where the effective medium is anisotropic and the corresponding helicity density of the averaged velocity field may differ significantly from zero indicating large-scale helical structures. As a direct consequence, we can observe in Figure 12 that also the development of the secondary
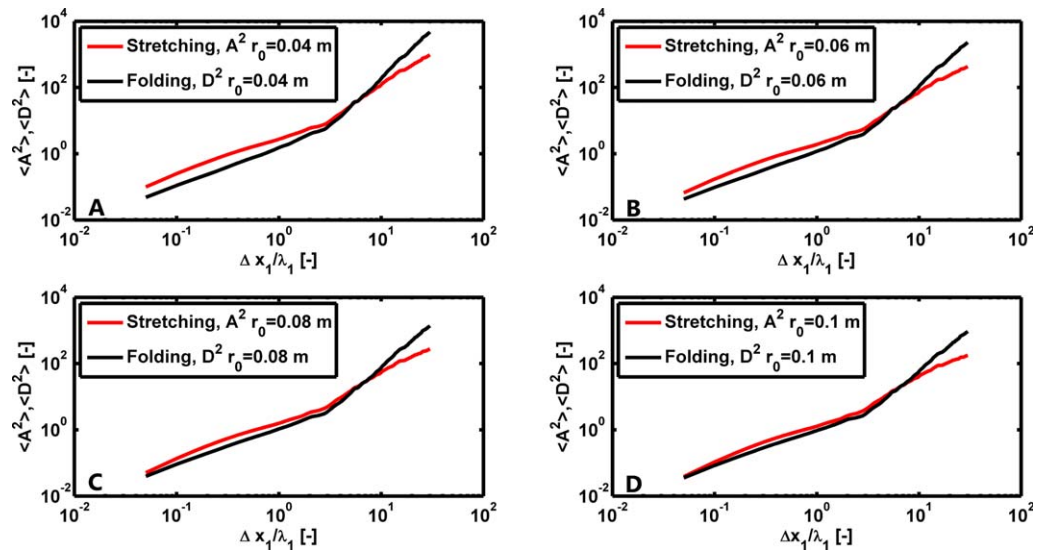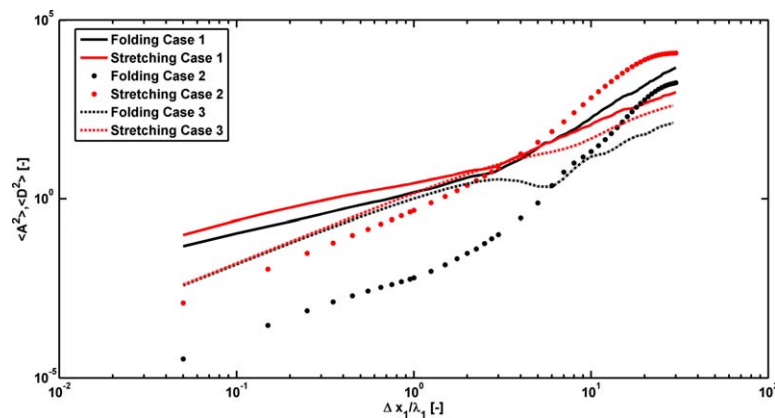
Figure 13. Mean values of A^2 (red) and D^2 (black) as a function of Δx_1 for different values of r_0: (a) $r_0 = 0.04$m, (b) $r_0 = 0.06$m, (c) $r_0 = 0.08$m, and (d) $r_0 = 0.1$m.

motion depends on the scale of the analysis and that it approaches the pattern observed in Figure 5 for a blockwise uniform effective conductivity field if the averaging scale ξ_1 increases.

5.2. Stretching and Folding

As described above, the topology of the flow field is altered by averaging and upscaling. However, although the helicity density is an important topological metric for the characterization of the flow field, recent studies have focused on characterizing stretching as an indicator of a plume's deformation to investigate how mixing is affected by advective processes [e.g., *Le Borgne et al.*, 2013; *Cirpka et al.*, 2011]. Therefore, it is worth analyzing stretching and folding mechanisms in three-dimensional porous media in the presence of helical streamlines. Figure 13 shows the stretching and folding metrics according to equations (11) and (12) for Case 1 considering four initial radii: $r_0 = 0.04, 0.06, 0.08, 1$m, one for each panel in the figure. The plots show averages over all possible locations of the circle center in the inlet face. The metrics of stretching ($<A^2>$) and folding ($<D^2>$) are shown versus the distance Δx_1. Notice that Δx_1 represents the distance between the plane where the source is placed (i.e., in our case $x_1 = 0$) and the plane at which we compute the deformation of the set of circles is computed. In all cases, more than six particles per circle are considered, which is the minimum suggested by *Kelley and Ouellette* [2011] to obtain statistically significant results. The maximum radius providing consistent results, in which folding is smaller than stretching at short distances, corresponds to the minimum correlation length, i.e., $r_{0,max} = \lambda_3$. The choice of the initial radius does not

significantly influence the rate of increase of both stretching and folding, which is in accordance with the results of *Kelley and Ouellette* [2011]. The deformation processes are stretching dominated at short distances, however, $<D^2>$ starts to increase more rapidly than $<A^2>$ for $\Delta x_1 \approx 2\lambda_1$, and it becomes the dominant component of the overall deformation for

Figure 14. Comparison of mean stretching (red) and folding (black) for Case 1 (continuous line), Case 2 (dots), and Case 3 (dash line).

$\Delta x_1 \approx 6\lambda_1$. This range corresponds to the transition zone where helical motion develops in Case 1 (see Figures 11 and 12). In this case, folding is a good indicator of the nonlinear deformation of a plume caused by the occurrence of helical structures at large scales.

Figure 14 compares the stretching and folding metrics of the fully resolved velocity field (Case 1) with those of the upscaled fields (Case 2 and Case 3). In all cases, the initial radius was $r_0 = 0.04$m. As expected, Case 1 shows different stretching and folding patterns than Cases 2 and 3, but with some relevant peculiarities that are worth a discussion. At a short distance from the inlet plane, the streamlines of Case 1 are more distorted than the streamlines of Cases 2 and 3. The spatial and Monte Carlo averaging, in Case 2, and the use of homogeneous, yet differently anisotropic, conductivity blocks in Case 3, lead to much smoother velocity fields, which attenuate small-scale streamline distortion with respect to Case 1. The crossover of folding is no longer observed in Cases 2 and 3 within the computational domain. The enhanced stretching and folding at distances larger than 60 m is clearly visible in Case 3 in the shaded region of Figure 7, showing the computed streamlines in a longer domain than in Cases 1 and 2. The streamlines originating from the left side of the injection plane require a longer distance than in Case 1 to deviate toward the center of the domain (see the progressive reduction of the white portion of the domain at distances larger than 60 m). In Case 2 for $\Delta x_1 > 6\lambda_1$, stretching becomes larger than in Case 1, showing that averaging may inflate the linear component of the deformation. In Case 3, at small to moderate distances ($\Delta x_1 \leq 0.5\lambda_1$), the two metrics assume almost the same value due to the sharp discontinuities in the velocity field at the edges of the blocks, which are not smoothed by the presence of the Tukey window function. Altogether, the increasing pattern of both stretching and folding is similar for the three cases; however, Case 2 provides a satisfying reproduction of the deformation patterns observed in Case 1, while Case 3 underestimates both stretching and folding, probably due to the homogeneity of the blocks.

6. Discussion and Conclusions

Previous studies focusing on flow topology and mixing considered two-dimensional flows in porous media [e.g., *de Barros et al.*, 2012], under steady state or transient conditions [e.g., *Sposito and Weeks*, 1998; *Piscopo et al.*, 2013]. Three-dimensional steady-state flows have been considered to be constrained on Lamb surfaces and hence characterized by a relatively simple topology [*Sposito*, 1994, 2001]. The results presented in this work point to the fact that flow topology and hence plume deformation is scale dependent and we have demonstrated that helical flows can occur also in locally isotropic, yet nonstationary, porous media at scales larger than some correlations lengths.

In particular, we have analyzed and compared a topological quantity, namely the helicity density and metrics of stretching and folding, applied to three related three-dimensional steady-state flow fields. We considered: (i) a fully resolved case of a locally isotropic heterogeneous three-dimensional porous medium with a nonstationary anisotropic covariance function of the hydraulic log conductivity; (ii) the flow field obtained by averaging along the longitudinal direction the mean velocity field obtained with 50 Monte Carlo realizations of the former fully resolved case; (iii) the flow field obtained by applying the blockwise homogeneous anisotropic effective conductivity tensor computed with the statistical parameters characterizing the fully resolved heterogeneous conductivity field. All three cases account for nonstationary anisotropy, here implemented as blockwise uniform orientation of the associated principal directions; in the first case, it is the anisotropy of the covariance function, in the second case an implicit anisotropy of local conductivity relating the specific-discharge vector obtained with a set of 50 Monte Carlo realizations, and in the third case an explicit anisotropy of local, yet upscaled, conductivity. Three-dimensional, nonstationary anisotropy is paramount for the phenomena discussed in the present study.

The most relevant feature of all three flow fields is the occurrence of macroscopically helical streamlines. This result was expected for the flow field of Case 3, in which a blockwise homogeneous anisotropic conductivity tensor has been used [*Bakker and Hemker*, 2002, 2004; *Hemker and Bakker*, 2006; *Hemker et al.*, 2004]. Since Case 3 has been constructed by upscaling the heterogeneous nonstationary conductivity field of Case 1, it is reasonable to expect that the macroscopic flow field of Case 1 shows a similar behavior. In fact, *Bakker and Hemker* [2002, 2004] argued that the blockwise anisotropy applied in their studies could be caused by small-scale features, which have been resolved in the present work.

At a first glance, the macroscopically helical flow field seems to be in contradiction with the fact that the helicity density must be zero everywhere in a heterogeneous, but locally isotropic conductivity field

[*Sposito*, 1994, 2001; *Kapoor*, 1997; *Bear*, 1972]. This apparent paradox is resolved when considering that the helicity density is a scale-dependent metric. At the smallest Darcy scale in a locally isotropic medium, streamlines are perpendicular to iso-potential surfaces, and the specific-discharge vector is orthogonal to its curl. At this scale, larger-scale anisotropy is not observable and hence the local (Darcy-scale) helicity density is zero. To evidence the larger-scale flow behavior, small-scale variability has to be averaged, that is, streamlines are locally straightened and iso-potential surfaces are smoothed. If the structure of heterogeneity is anisotropic, the smoothed streamlines may no more be perpendicular to the smoothed iso-potential surfaces (indicating an anisotropic effective conductivity tensor), and the smoothed specific-discharge vector may no more be orthogonal to its curl. That is, the upscaled velocity field may exhibit nonzero helicity density, which is the key outcome of the present analysis. Scale dependency of flow properties is common in porous media literature, however, the relevance of nonstationarity in the statistical properties of the conductivity field, as well as of the boundary conditions for the helicity density pose a challenge in the analytical upscaling of this topological metric. Indeed, nonzero upscaled helicity density will be particularly pronounced when the anisotropy of heterogeneity is nonstationary, that is, when the principal directions of anisotropy vary in space.

In his pioneering works, *Sposito* [2001, 1994] showed that helicity density in a statistically stationary and locally isotropic heterogeneous conductivity field is everywhere zero, irrespective to the degree of heterogeneity. In our work, we extended this analysis showing that certain statistically nonstationary conductivity fields develop helical structures at scales larger than the Darcy scale, yet with local helicity density equal to zero. This helical structure is preserved only if a proper upscaling is applied to the velocity field. For the properly upscaled velocity field, helicity density differs from zero and can be used as a metric of plume deformation and ultimately as an approximate metric of mixing. In *Cirpka et al.* [2015], we show how large-scale helical flow can significantly enhance transverse dispersion in comparison to statistically stationary formations, where lateral solute fluxes are limited. In the present study, helical streamlines can occur already at scales comparable to the correlation length in the x_1 direction. Helicity characterization in the field is of course difficult as we discuss also in *Cirpka et al.* [2015]. Outcrop studies, however, have indicated that nonstationary anisotropy occurs very often in nature. These results points to the need of improved techniques for the characterization of the shape and orientation of the geological structures in the subsurface. Indeed, the potential occurrence of helical streamlines can be verified at the field scale if also the geometry and eventually the local anisotropy of the heterogeneous subsurface structures is well characterized. Similar considerations were also reached by *Stauffer* [2007] analyzing in a numerical exercise the impact of a single highly permeable inclusion with inclined bedding instead of using topological arguments. Notice that the approaches of *Stauffer* [2007], *Bakker and Hemker* [2002, 2004], *Hemker and Bakker* [2006], and *Hemker et al*. [2004] require a numerical integration of the flow field to construct streamlines and to observe a posteriori the occurrence of helical flows. This step may be challenging from a numerical point of view if the helicity density is nonzero [*Holm and Kimura*, 1991]. Analyzing the topology of the flow field can predict a priori properties of the streamlines by knowing only the velocity field. Furthermore, this study shows that the helicity density, as well as other topological metrics such as the Okubo-Weiss parameter [*de Barros et al*., 2012], should be quantified at the appropriate scale of the phenomena of interest. In field-scale studies, it is of little interest to compute the helicity density for the local heterogeneous field, but it is a relevant metric at scales where helical structures can be expected (i.e., at scales larger than a few correlation lengths where porous media can be modeled as anisotropic).

Preserving local flow topology in three-dimensional numerical simulations is a challenging task. The cell-centered Finite Volume Method with harmonic averaging of the cell-conductivities applied in this study introduces artifacts of the local velocity field, namely an apparent anisotropy of the equivalent conductivity tensor and a nonzero helicity density even in a conductivity field that was meant to be locally isotropic. This is an inherent problem of several discretization schemes, because discretization itself involves upscaling, and, as we have seen, topology changes with scale. The artifacts depend on the variance of the log conductivity and vanish upon refinement of the computational grid.

We further characterized the deformation introduced in the plume by the flow field by analyzing stretching and folding. We have observed that, at short distances from the source, stretching is dominating over folding, and that these two quantities display a similar pattern for all three cases considered. However, in the fully resolved nonstationary case, the transition from a stretching-dominated to a folding-dominated

behavior occurs earlier than in the other two cases. This is due to the higher flow variability in the fully resolved case in comparison to the other two cases. Since stretching and folding facilitates solute mixing across plume interfaces, we infer from the analyses of stretching and folding metrics of the fully resolved field over the upscaled ones that the interaction between the large-scale secondary motion and the small-scale heterogeneity of the flow field contributes to efficient mixing.

The analyses of helicity density, stretching and folding metrics are useful for gaining further understanding on how flow topology influences local concentration gradients through geometrical deformation of streamlines, yet they do not consider the relevant effect of local dispersion on solute transport in porous media. In a companion paper, focusing on solute transport, we explicitly solve the advection-dispersion equation to analyze how the deformation of the plume due to the helical characteristics of the flow field, discussed in the present work, influence mixing and plume dilution [*Cirpka et al.*, 2015]. The helicity density provides a local description of the flow field which allows to investigate at which scale macroscopic helical structures can be detected; stretching and folding are kinematic descriptors of mixing and concern the mean deformation of stream tubes at different spatial scales and thus they are global indicators of mixing processes. In particular, folding provides results which are in agreement with the interpretation of the scale dependence of the helicity density, showing a faster increase in the nonlinear component of the deformation when helical streamlines occur. Therefore, folding is informative in order to identify at which scale different phenomena are relevant. Notice that, while the application of these topological and kinematic metrics are not common in groundwater literature, they have been used in other branches of fluid dynamics at various scales. For example, *Stroock et al.* [2002] has shown how helical flow fields lead to larger stretching and folding, and hence mixing, in microchannels at low Reynolds numbers. In particular, the helicity is relevant since it is an invariant of the flow, which expresses the mutual linking of the trajectories of the vorticity field [*Arnold and Khesin*, 1998]. Further studies analyzing the occurrence of zones with nonzero helicity density may be useful to determine when helicity is an indicator for the potential occurrence of helical flow in stationary three-dimensional domains. In addition, stretching and folding have been useful in characterizing mixing for transient two-dimensional chaotic flows in time and space [*Kelley and Ouellette*, 2011]. In particular, the similarity between our results obtained for steady state nonstationary anisotropic fields and the results reported by *Kelley and Ouellette* [2011] is striking and shows that the analysis of these two metrics is relevant in order to identify the scales at which linear and nonlinear deformations are dominant. This is important since, as shown in *Cirpka et al.* [2015], higher folding can be related with higher dilution. Hence, further investigations should be conducted to establish a rigorous parallelism between steady state three-dimensional flow fields in porous media and two-dimensional transient chaotic flows.

The outcomes of this work are of practical interest, since natural formations are inherently heterogeneous and may show anisotropy in the local hydraulic properties at different scales, as observed in multiscale sedimentary structures ranging from packing of nonspherical particles, via graded bedding, cross bedding to sedimentation processes in braided river environments. In such environments, relevant flow-topological features, such as streamline twisting can be observed only in three-dimensional setups. A direct consequence of the complex flow topology identified in this work, is a significant and more effective mixing enhancement in three-dimensional domains than in two-dimensional ones, in particular in the transverse directions perpendicular to mean flow. While the impact of sedimentary features on solute transport has been investigated in the past [*Fogg*, 1986; *Riva et al.*, 2008; *Sun et al.*, 2008], this study aimed at showing that the physical processes leading to potential mixing enhancement are different if nonstationarity and local anisotropy in hydraulic properties of 3-D domains are considered. These effects go beyond the expected increase of dilution by switching from two to three dimensions in traditionally analyzed stationary conductivity fields [*Kitanidis*, 1994; *Rubin*, 2003]. A detailed investigation of these aspects is provided in the companion paper [*Cirpka et al.,* 2015].

References

Alyamani, M. S., and Z. Sen (1993), Determination of hydraulic conductivity from complete grain-size distribution curves, *Ground Water*, *31*(4), 551–555, doi:10.1111/j.1745-6584.1993.tb00587.x.

Arnold, V., and B. Khesin (1998), *Topological Methods in Hydrodynamics*, Springer, N. Y.

Bagtzoglou, A. C., and P. M. Oates (2007), Chaotic advection and enhanced groundwater remediation, *J. Mater. Civ. Eng.*, *19*, 75–83, doi:10.1061/(ASCE)0899-1561(2007)19:1(75).

Bakker, M., and K. Hemker (2002), A dupuit formulation for flow in layered, anisotropic aquifers, *Adv. Water Resour.*, *25*, 747–754.

Bakker, M., and K. Hemker (2004), Analytic solutions for groundwater whirls in box-shaped, layered anisotropic aquifers, *Adv. Water Resour.*, *27*, 1075–1086.

Battiato, I., D. Tartakovsky, A. Tartakovsky, and T. Scheibe (2011), Hybrid models of reactive transport in porous and fractured media, *Adv. Water Resour.*, *34*(9), 1140–1150, doi:10.1016/j.advwatres.2011.01.012.

Bear, J. (1972), *Dynamics of Fluids in Porous Media*, Elsevier, N. Y.

Bear, J., and G. Dagan (1965), The relationship between solutions of flow problems in isotropic and anisotropic soils, *J. Hydrol.*, *3*(2), 88–96, doi:10.1016/0022-1694(65)90002-8.

Bellin, A., P. Salandin, and A. Rinaldo (1992), Simulation of dispersion in heterogeneous porous formations: Statistics, first-order theories, convergence of computations, *Water Resour. Res.*, *28*(9), 2211–2227.

Blatt, H., G. Middleton, and R. Murray (1980), *Origin of Sedimentary Rocks*, Prentice Hall, Englewood Cliffs, N. J.

Bouwer, H., and R. C. Rice (1976), A slug test for determining hydraulic conductivity of unconfined aquifers with completely or partially penetrating wells, *Water Resour. Res.*, *12*(3), 423–428, doi:10.1029/WR012i003p00423.

Cainelli, O., A. Bellin, and M. Putti (2012), On the accuracy of classic numerical schemes for modeling flow in saturated heterogeneous formations, *Adv. Water Resour.*, *47*, 43–55, doi:10.1016/j.advwatres.2012.06.016.

Chiogna, G., and A. Bellin (2013), Analytical solution for reactive solute transport considering incomplete mixing within a reference elementary volume, *Water Resour. Res.*, *49*, 2589–2600, doi:10.1002/wrcr.20200.

Chiogna, G., O. A. Cirpka, P. Grathwohl, and M. Rolle (2011a), Relevance of local compound-specific transverse dispersion for conservative and reactive mixing in heterogeneous porous media, *Water Resour. Res.*, *47*, W07540, doi:10.1029/2010WR010270.

Chiogna, G., O. A. Cirpka, P. Grathwohl, and M. Rolle (2011b), Transverse mixing of conservative and reactive tracers in porous media: Quantification through the concepts of flux-related and critical dilution indices, *Water Resour. Res.*, *47*, W02505, doi:10.1029/2010WR009608.

Chiogna, G., D. L. Hochstetler, A. Bellin, P. K. Kitanidis, and M. Rolle (2012), Mixing, entropy and reactive solute transport, *Geophys. Res. Lett.*, *39*, L20405, doi:10.1029/2012GL053295.

Chiogna, G., M. Rolle, A. Bellin, and O. A. Cirpka (2014), Helicity and flow topology in three dimensional anisotropic porous media, *Adv. Water Resour.*, *73*, 134–143, doi:10.1016/j.advwatres.2014.06.017.

Cirpka, O. A., F. P. J. de Barros, G. Chiogna, M. Rolle, and W. Nowak (2011), Stochastic flux-related analysis of transverse mixing in two-dimensional heterogeneous porous media, *Water Resour. Res.*, *47*, W06515, doi:10.1029/2010WR010279.

Cirpka, O. A., G. Chiogna, M. Rolle, and A. Bellin (2015), Transverse mixing in three-dimensional nonstationary anisotropic heterogeneous porous media, *Water Resour. Res.*, *51*, doi:10.1002/2014WR015331.

Dagan, G. (1989), *Flow and Transport in Porous Formations*, Springer, N. Y.

Dagan, G., A. Fiori, and I. Jankovic (2013), Upscaling of flow in heterogeneous porous formations: Critical examination and issues of principle, *Adv. Water Resour.*, *51*, 67–85.

de Barros, F. P. J., M. Dentz, J. Koch, and W. Nowak (2012), Flow topology and scalar mixing in spatially heterogeneous flow fields, *Geophys. Res. Let.*, *39*, L08404, doi:10.1029/2012GL051302.

Dietrich, C., and G. Newsam (1993), A fast and exact method for multidimensional Gaussian stochastic simulations, *Water Resour. Res.*, *29*(8), 2861–2869.

Durlofsky, L. J. (1992), Representation of grid block permeability in coarse scale models of randomly heterogeneous porous media, *Water Resour. Res.*, *28*(7), 1791–1800.

Falk, M. L., and J. S. Langer (1998), Dynamics of viscoplastic deformation in amorphous solids, *Phys. Rev. E*, *57*(6), 7192–7205.

Fogg, G. L. (1986), Groundwater flow and sand body interconnectedness in a thick, multiple-aquifer system, *Water Resour. Res.*, *22*(5), 679–694, doi:10.1029/WR022i005p00679.

Friedman, S. P., and N. A. Seaton (1996), On the transport properties of anisotropic networks of capillaries, *Water Resour. Res.*, *32*(2), 339–347, doi:10.1029/95WR02830.

Gelhar, L. W. (1993), *Stochastic Subsurface Hydrology*, Prentice Hall, Englewood Cliffs, N. J.

Gelhar, L. W., and C. L. Axness (1983), Three-dimensional stochastic analysis of macrodispersion in aquifers, *Water Resour. Res.*, *19*(1), 161–180.

Guin, A., R. Ramanathan, R. W. Ritzi, D. F. Dominic, I. A. Lunt, T. D. Scheibe, and V. Freedman (2010), Simulating the heterogeneity in braided channel belt deposits: 2. Examples of results and comparison to natural deposits, *Water Resour. Res.*, *46*, W04516, doi:10.1029/2009WR008112.

Hantush, M. S., and R. G. Thomas (1966), A method for analyzing a drawdown test in anisotropic aquifers, *Water Resour. Res.*, *2*(2), 281–285, doi:10.1029/WR002i002p00281.

Heinz, J., and T. Aigner (2003), Hierarchical dynamic stratigraphy in various quaternary gravel deposits, Rhine glacier area (SW Germany): Implications for hydrostratigraphy, *Int. J. Earth Sci.*, *92*(6), 923–938, doi:10.1007/s00531-003-0359-2.

Heinz, J., S. Kleineidam, G. Teutsch, and T. Aigner (2003), Heterogeneity patterns of Quaternary glaciofluvial gravel bodies (SW-Germany): Application to hydrogeology, *Sediment. Geol.*, *158*(1-2), 1–23, doi:10.1016/S0037-0738(02)00239-7.

Hemker, K., and M. Bakker (2006), Analytical solutions for whirling groundwater flow in two-dimensional heterogeneous anisotropic aquifers, *Water Resour. Res.*, *42*, W12419, doi:10.1029/2006WR004901.

Hemker, K., E. van den Berg, and M. Bakker (2004), Ground water whirls, *Ground Water*, *42*(2), 234–242.

Herrera, P. A., A. J. Valocchi, and R. D. Beckie (2010), A multidimensional streamline-based method to simulate reactive solute transport in heterogeneous porous media, *Adv. Water Resour.*, *33*(7), 711–727, doi:10.1016/j.advwatres.2010.03.001.

Holm, D., and Y. Kimura (1991), Zero-helicity Lagrangian kinematics of three-dimensional advection, *Phys. Fluids A*, *3*, 1033–1038.

Hsieh, P. A., S. P. Neuman, G. K. Stiles, and E. S. Simpson (1985), Field determination of the three-dimensional hydraulic conductivity tensor of anisotropic media: 2. Methodology and application to fractured rocks, *Water Resour. Res.*, *21*(11), 1667–1676, doi:10.1029/WR021i011p01667.

Indelman, P., and G. Dagan (1993), Upscaling of permeability of anisotropic heterogeneous formations: 1. The general framework, *Water Resour. Res.*, *29*(4), 917–923.

Jankovic, I., A. Fiori, and G. Dagan (2003), Effective conductivity of an isotropic heterogeneous medium of lognormal conductivity distribution, *Multiscale Model. Simul.*, *1*, 40–56.

Jankovic, I., A. Fiori, and G. Dagan (2013), Effective conductivity of isotropic highly heterogeneous formations: Numerical and theoretical issues, *Water Resour. Res.*, *49*, 1178–1183, doi:10.1029/2012WR012441.

Kapoor, V. (1997), Vorticity in three-dimensionally random porous media, *Transp. Porous Media*, *26*, 109–119.

Kelley, D. H., and N. T. Ouellette (2011), Separating stretching from folding in fluid mixing, *Nat. Phys.*, *7*, 477–480.

Kim, J.-H., J. Ochoa, and S. Whitaker (1987), Diffusion in anisotropic porous media, *Transp. Porous Media*, *2*(4), 327–356, doi:10.1007/BF00136440.

Kitanidis, P. K. (1994), The concept of the dilution index, *Water Resour. Res.*, *30*(7), 2011–2026.

Kostic, B., and T. Aigner (2007), Sedimentary architecture and 3d ground-penetrating radar analysis of gravelly meandering river deposits (Neckar Valley, sw Germany), *Sedimentology*, *54*(4), 789–808, doi:10.1111/j.1365-3091.2007.00860.x.

Le Borgne, T., M. Dentz, D. Bolster, J. Carrera, J.-R. de Dreuzy, and P. Davy (2010), Non-fickian mixing: Temporal evolution of the scalar dissipation rate in heterogeneous porous media, *Adv. Water Resour.*, *33*(12), 1468–1475, doi:10.1016/j.advwatres.2010.08.006.

Le Borgne, T., M. Dentz, and E. Villermaux (2013), Stretching, coalescence, and mixing in porous media, *Phys. Rev. Lett.*, *110*, 204501, doi:10.1103/PhysRevLett.110.204501.

Li, L., H. Zhou, and J. J. Gómez-Hernández (2010), Steady-state saturated groundwater flow modeling with full tensor conductivities using finite differences, *Comput. Geosci.*, *36*(10), 1211–1223.

Liu, J.-G., and W.-C. Wang (2004), Energy and helicity preserving schemes for hydro- and magnetohydro-dynamics flows with symmetry, *J. Comput. Phys.*, *200*(1), 8–33, doi:10.1016/j.jcp.2004.03.005.

McLaughlin, D., and L. R. Townley (1996), A reassessment of the groundwater inverse problem, *Water Resour. Res.*, *32*(5), 1131–1161.

Mial, A. D. (1996), *The Geology of Fluvial Deposits: Sedimentary Facies, Basin Analysis, and Petroleum Geology*, Springer, Berlin.

Milton, G. W. (2002), *Theory of Composites*, Cambridge Univ. Press, Cambridge, U. K.

Moffatt, H., and A. Tsinober (1992), Helicity in laminar and turbulent flow, *Ann. Rev. Fluid Mech.*, *24*, 281–312.

Neuman, S. P., and V. Di Federico (2003), Multifaceted nature of hydro- geologic scaling and its interpretation, *Rev. Geophys.*, *41*(3), 1014, doi:10.1029/2003RG000130.

Neupauer, R. M., J. D. Meiss, and D. C. Mays (2014), Chaotic advection and reaction during engineered injection and extraction in heterogeneous porous media, *Water Resour. Res.*, *50*, 1433–1447, doi:10.1002/2013WR014057.

Ottino, J. (1989), *The Kinematics of Mixing: Stretching, Chaos, and Transport*, Cambridge Univ. Press, Cambridge, U. K.

Paleologos, E. K., S. Neuman, and D. Tartakovsky (1996), Effective hydraulic conductivity of bounded, strongly heterogeneous porous media, *Water Resour. Res.*, *32*(5), 1333–1341.

Piscopo, A. N., R. M. Neupauer, and D. C. Mays (2013), Engineered injection and extraction to enhance reaction for improved in situ remediation, *Water Resour. Res.*, *49*, 3618–3625, doi:10.1002/wrcr.20209.

Poeter, E. P., and D. R. Gaylord (1990), Influence of aquifer heterogeneity on contaminant transport at the hanford site, *Ground Water*, *28*, 900–909.

Pollock, D. W. (1988), Semianalytical computation of path lines for finite-difference models, *Ground Water*, *26*(6), 743–750.

Ramanathan, R., A. Guin, R. W. Ritzi, D. F. Dominic, V. Freedman, T. D. Scheibe, and I. A. Lunt (2010), Simulating the heterogeneity in braided channel belt deposits: 1. A geometric-based methodology and code, *Water Resour. Res.*, *46*, W04515, doi:10.1029/2009WR008111.

Renard, P., and G. de Marsily (1997), Calculating effective permeability: A review, *Adv. Water Resour.*, *20*, 253–278.

Ritzi, R. W., and R. M. Allen-King (2007), Why did Sudicky [1986] find an exponential-like spatial correlation structure for hydraulic conductivity at the Borden research site?, *Water Resour. Res.*, *43*, W01406, doi:10.1029/2006WR004935.

Riva, M., A. Guadagnini, D. Fernandez-Garcia, X. Sanchez-Vila, and T. Ptak (2008), Relative importance of geostatistical and transport models in describing heavily tailed breakthrough curves at the Lauswiesen site, *J. Contam. Hydrol.*, *101*(1-4), 1–13, doi:10.1016/j.jconhyd.2008.07.004.

Rolle, M., and P. Kitanidis (2014), Effects of compound-specific dilution on transient transport and solute breakthrough: A pore-scale analysis, *Adv. Water Resour.*, *71*, 186–199, doi:10.1016/j.advwatres.2014.06.012.

Rolle, M., C. Eberhardt, G. Chiogna, O. A. Cirpka, and P. Grathwohl (2009), Enhancement of dilution and transverse reactive mixing in porous media: Experiments and model-based interpretation, *J. Contam. Hydrol.*, *110*(3-4), 130–142, doi:10.1016/j.jconhyd.2009.10.003.

Rolle, M., G. Chiogna, D. L. Hochstetler, and P. K. Kitanidis (2013), On the importance of diffusion and compound-specific mixing for groundwater transport: An investigation from pore to field scale, *J. Contam. Hydrol.*, *153*, 51–68, doi:10.1016/j.jconhyd.2013.07.006.

Ronayne, M. J., S. M. Gorelick, and C. Zheng (2010), Geological modeling of submeter scale heterogeneity and its influence on tracer transport in a fluvial aquifer, *Water Resour. Res.*, *46*, W10519, doi:10.1029/2010WR009348.

Rubin, Y. (2003), *Applied Stochastic Hydrogeology*, Oxford Univ. Press, Oxford, U. K.

Sanchez-Vila, X., J. P. Girardi, and J. Carrera (1995), A synthesis of approaches to upscaling of hydraulic conductivities, *Water Resour. Res.*, *31*(4), 867–882.

Sanchez-Vila, X., A. Guadagnini, and J. Carrera (2006), Representative hydraulic conductivities in saturated groundwater flow, *Rev. Geophys.*, *44*, RG3002, doi:10.1029/2005RG000169.

Sposito, G. (1994), Steady groundwater flow as a dynamical system, *Water Resour. Res.*, *20*(8), 2395–2401.

Sposito, G. (2001), Topological groundwater hydrodynamics, *Adv. Water Resour.*, *24*, 793–801.

Sposito, G., and S. W. Weeks (1998), Tracer advection by steady groundwater flow in a stratified aquifer, *Water Resour. Res.*, *34*(5), 1051–1059, doi:10.1029/98WR00009.

Stauffer, F. (2007), Impact of highly permeable sediment units with inclined bedding on solute transport in aquifers, *Adv. Water Resour.*, *30*(11), 2194–2201, doi:10.1016/j.advwatres.2007.04.008.

Stroock, A. D., S. K. W. Dertinger, A. Ajdari, I. Mezi, H. A. Stone, and G. M. Whitesides (2002), Chaotic mixer for microchannels, *Science*, *295*(5555), 647–651, doi:10.1126/science.1066238.

Sun, A. Y., R. W. Ritzi, and D. W. Sims (2008), Characterization and modeling of spatial variability in a complex alluvial aquifer: Implications on solute transport, *Water Resour. Res.*, *44*, W04402, doi:10.1029/2007WR006119.

Theis, C. V. (1935), The relation between the lowering if the piezometric surface and the rate and duration of discharge of a well using groundwater storage, *Trans. AGU*, *2*, 519–524.

Tukey, J. W. (1967), An introduction to the calculations of numerical spectrum analysis, in Harris, B. (ed.), *Spectral Analysis of Time Series*, New York: Wiley, pp. 25–46.

Weeks, S. W., and G. Sposito (1998), Mixing and stretching efficiency in steady and unsteady groundwater flows, *Water Resour. Res.*, *34*(12), 3315–3322, doi:10.1029/98WR02535.

Wen, X.-H., and J. Gomez-Hernandez (1996), Upscaling hydraulic conductivities in porous media: An overview, *J. Hydrol.*, *183*, 181–211.

Werth, C. J., O. A. Cirpka, and P. Grathwohl (2006), Enhanced mixing and reaction through flow focusing in heterogeneous porous media, *Water Resour. Res.*, *42*, W12414, doi:10.1029/2005WR004511.

Zhou, H., L. Li, and J. Jaime Gómez-Hernández (2010), Three-dimensional hydraulic conductivity upscaling in groundwater modeling, *Comput. Geosci.*, *36*(10), 1224–1235.